

Dual-Band Perovskite Bulk Heterojunction Self-Powered Photodetector for Encrypted Communication and Imaging

Fa Cao, Tingting Yan, Ziqing Li, Limin Wu,* and Xiaosheng Fang*

Self-powered, dual-band photodetection of electromagnetic signals promises wide photoelectric applications in imaging, communication, environmental monitoring, and rescue. However, most reported dual-band photodetectors (PDs) based on various heterojunctions are realized by complex fabrication processes, which may introduce defects in the depletion layer. Here, first, a self-powered dual-band PD based on lead-free perovskite bulk heterojunction ($\text{Cs}_3\text{Bi}_2\text{Br}_9/\text{Cs}_3\text{BiBr}_6$) fabricated by a one-step spatial confinement method is demonstrated. Its two peaks of self-powered responsivities are 59.4 mA W^{-1} at 360 nm and 3.09 mA W^{-1} at 450 nm. A high on/off ratio (18881), fast response speed (rise time 200 ns; decay time 1.09 μs), high detectivity (1.2×10^{12} Jones), and cycle stability are realized under UV band, which exceeds most reported state-of-the-art lead-free halide perovskite PDs. The dual-band PD is suitable for encrypted communication and image sensing. This research represents a new frontier in the search for novel dual-band high-performance PDs based on lead-free perovskite bulk heterojunction fabricated by low-cost and simple fabrication methods.

respond to different wavelengths of light. Dual-band optical signal is modulated in different forms which increases the difficulties of the signal decoding if the correct modulation wavelength is not known. Furthermore, the third generation of imaging technology also calls for low-cost, high-resolution imaging with dual-band imaging capability.^[2] PDs with multi-spectral detection capability can address these requirements to a certain extent.^[3]

Over the past few decades, self-powered multispectral photodetection has garnered much attention due to its capability to detect more than one band, leading itself to potential application in imaging, remote-sensing, missile warning, and encrypted communications, etc.^[4–8] Accordingly, researchers have expanded the inherent detection range from the absorption limit of one single material by constructing of heterojunctions with different absorption

ranges. A number of self-powered ultraviolet (UV)/UV,^[9] UV/visible,^[10] and UV/infrared^[2] dual-band PDs have been proposed. However, these multi-band PDs rely on two different materials, which could experience lattice and thermal mismatch between the semiconductors during epitaxial growth.^[2,11] Therefore, there is a growing demand for simpler and more cost-effective approaches to fabricating dual-band photodetectors.

Recently, metal halide perovskites have attracted worldwide research attention because of their diverse facile and easy synthesis methods, tunable direct bandgap, high carrier mobility, large optical absorption coefficient, and high sensitivity and stability for photon detection.^[12–18] However, the most-researched lead-based perovskites are limited for practical applications because of the toxicity of lead.^[19,20] Tin has been considered as a promising alternative for lead-free perovskites because of their similar atomic radius.^[21] However, the oxidation of Sn^{2+} to Sn^{4+} makes the tin-based perovskites unstable in air. Alternatively, bismuth (Bi)-based perovskites have been found possessing long-term stability and featuring excellent photosensitivity, so they have obtained more research attention and are regarded as promising lead-free perovskite materials.^[22]

Among these materials, compounds of cesium bismuth halides are particularly interesting because of their structural diversity.^[23] Cesium bismuth bromide compounds with different structures and stoichiometry have been reported: $\text{Cs}_3\text{Bi}_2\text{Br}_9$, and Cs_3BiBr_6 . Researchers have investigated the photodetection properties of $\text{Cs}_3\text{Bi}_2\text{Br}_9$ (direct bandgap $\approx 2.6 \text{ eV}$) by combining it with various other semiconductors. However,

1. Introduction


Photodetectors (PDs) with the ability to convert optical signals into electrical signals which can realize the transmission of information, exhibiting great possibilities for the development of Internet of things devices.^[1] However, traditional PDs, which respond only to a single frequency band, may face the risk of signal leakage if the wavelength of the propagating signal is leaked and broadband PDs face signal interference since it can

F. Cao, T. T. Yan, L. M. Wu, X. S. Fang
Department of Materials Science
Fudan University
Shanghai 200433, P. R. China
E-mail: lmw@fudan.edu.cn; xshfang@fudan.edu.cn

F. Cao
Zhangjiang Fudan International Innovation Center
Shanghai 201210, P. R. China

Z. Q. Li, X. S. Fang
Institute of Optoelectronics
Fudan University
Shanghai 200433, P. R. China

L. M. Wu
College of Chemistry and Chemical Engineering
Inner Mongolia University
Hohhot 010021, P. R. China

 The ORCID identification number(s) for the author(s) of this article can be found under <https://doi.org/10.1002/adom.202200786>.

DOI: 10.1002/adom.202200786

there is no report regarding dual-band photodetection PDs based on $\text{Cs}_3\text{Bi}_2\text{Br}_9$,^[23,24] Cs_3BiBr_6 (direct bandgap 3.2–3.4 eV), on the other hand, has been discovered only recently and there is disagreement over its crystal structure. Because the energy bandgaps of $\text{Cs}_3\text{Bi}_2\text{Br}_9$ and Cs_3BiBr_6 are different and they have the same constituent elements and preparation methods, therefore, it is feasible to make $\text{Cs}_3\text{Bi}_2\text{Br}_9/\text{Cs}_3\text{BiBr}_6$ (CBB) bulk heterojunction in one step to realize self-powered dual-band PDs.

Here, we demonstrated the fabrication of a high-performance, self-powered, and dual-band perovskite (CBB) bulk heterojunction by a one-step spatial confinement method. The Au-CBB-ITO PD possesses a UV main band (360 nm) with a self-powered peak responsivity of 59.4 mA W^{-1} and a blue sub-band (450 nm) with a self-powered peak responsivity of 4.09 mA W^{-1} . A high on/off ratio (18881), fast response speed (rise time 200 ns; decay time 1.09 μs), high detectivity (1.2×10^{12} Jones), high external quantum efficiency (EQE; 20.37%), and cycle stability were realized under the UV band at 0 V bias. The dual-band PD can be well applied in encrypted communications and

image sensing systems. Our research represents a new frontier in the search for novel dual-band high-performance PDs based on lead-free perovskite bulk heterojunction materials with structural diversity.

2. Results and Discussion

The fabrication process, PD structure, and device characterization method are shown in the Supporting Information, experimental section (Figure S1–S3, Supporting Information). The morphology, size, and growth mechanism of CBB micron flakes are also illustrated in the Supporting Information (Figure S4 and S5, Supporting Information). The CBB X-ray diffraction pattern is displayed in Figure 1a. The diffraction peaks with 2θ of 18.21°, 27.31°, 32.44°, 39.15°, 46.17°, 56.13°, 66.58°, and 78.07° are indexed to the (002), (003), (202), (104), (005), (006), (007) and (008) crystal facets of the hexagonal-phase $\text{Cs}_3\text{Bi}_2\text{Br}_9$ (JCPDS # 44–0714), demonstrating its [001] growth direction. Three small peaks centered at 19.24°, 24.39°, and 28.51° are

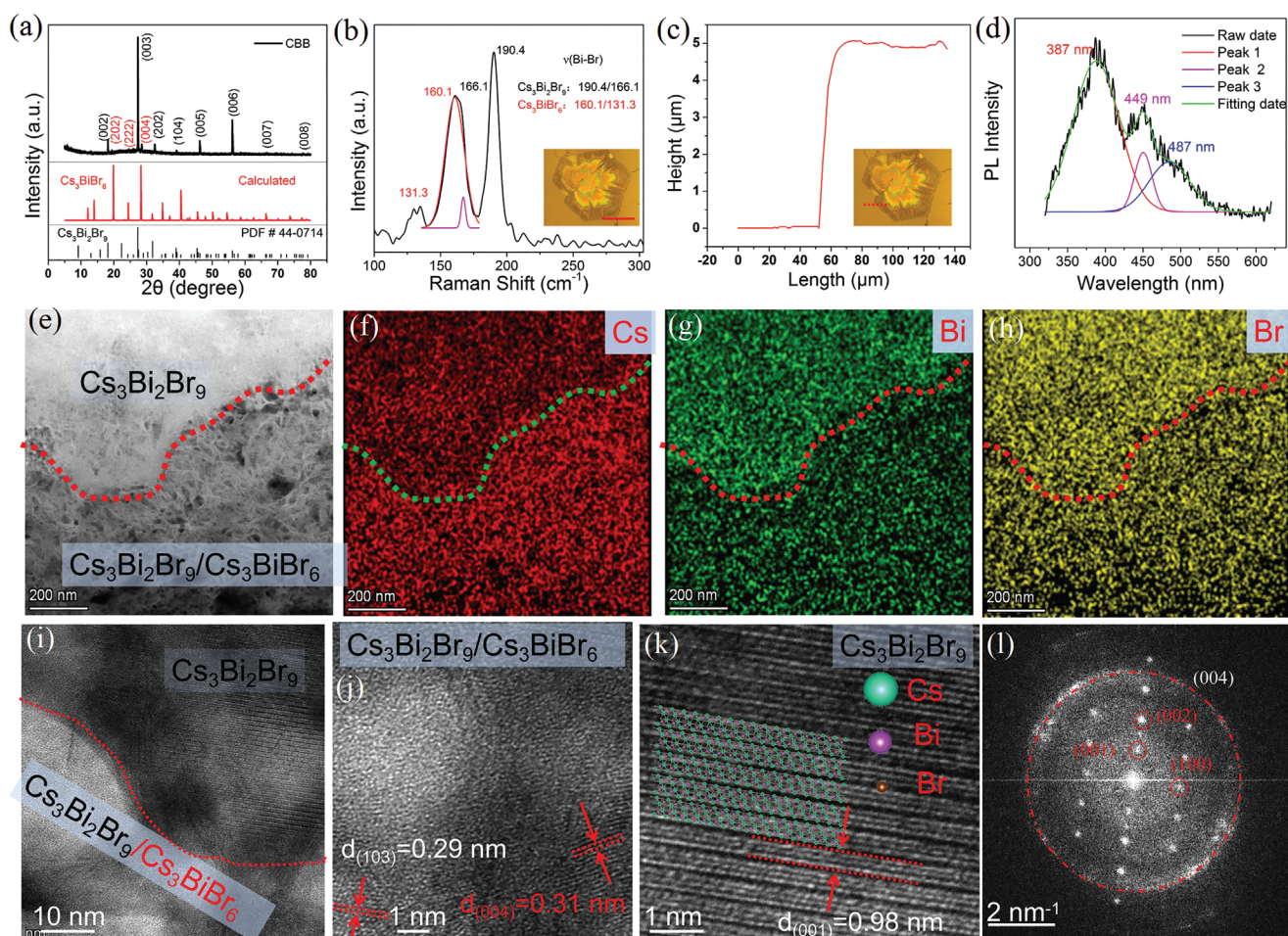


Figure 1. a) X-ray diffraction (XRD) pattern of $\text{Cs}_3\text{Bi}_2\text{Br}_9/\text{Cs}_3\text{BiBr}_6$ micron flakes and the calculated Cs_3BiBr_6 XRD pattern. b) Raman spectra of $\text{Cs}_3\text{Bi}_2\text{Br}_9/\text{Cs}_3\text{BiBr}_6$ micron flakes; the inset shows the corresponding optical image (scale bar 200 μm). c) Height profile along the line shown in the inset. d) PL spectra of $\text{Cs}_3\text{Bi}_2\text{Br}_9/\text{Cs}_3\text{BiBr}_6$. e) TEM image of the interface of $\text{Cs}_3\text{Bi}_2\text{Br}_9$ and Cs_3BiBr_6 . f–h) EDS maps corresponding to (e). i) HRTEM image of the interface of $\text{Cs}_3\text{Bi}_2\text{Br}_9/\text{Cs}_3\text{BiBr}_6$. j,k) Enlarged view corresponding to the upper right and lower left zone of (i), respectively. l) Selected area electron diffraction SAED patterns corresponding to (i).

ascribed to the (202), (222), and (004) crystal facets of Cs₃BiBr₆ (space group: p1) as calculated by VESTA software. No other miscellaneous phases and elements proved by XPS data (Figure S6, Supporting Information) were found, indicating the purity of the bulk heterojunction.

Raman spectroscopy was also used to confirm the bulk heterojunction of Cs₃Bi₂Br₉ and Cs₃BiBr₆. Three main peaks located at 131.3, 161.2, and 190.4 cm⁻¹ are observed from 100 to 300 cm⁻¹, and the peaks centered at 161.2 cm⁻¹ can be fitted by two Gaussian peaks lies in 160.1 and 166.1 cm⁻¹.^[23,24] Sharp peaks at 190.4 and 166.1 cm⁻¹ agrees closely with the Raman spectrum from the Cs₃Bi₂Br₉, corresponding to the A_{1g} and E_g normal modes of Bi-Br vibrations in the corner-sharing [BiBr₆]³⁻ octahedral, respectively. Although Cs₃BiBr₆ also contains [BiBr₆]³⁻ complexes, the octahedral are isolated and do not share corners, resulting in two peaks centered at 161.2 and 131.3 cm⁻¹; they are quite different from those detected in Cs₃Bi₂Br₉. The length of the CBB micron flakes reached 600 μm (inset of Figure 1b) with a thickness of ≈5 μm (Figure 1c). Figure 1d shows the PL spectrum of the CBB micron flakes with a broad peak from 340–530 nm. The broad peak can be fitted by three peaks centered at 387, 449, and 487 nm, which can be respectively ascribed to the direct bandgap electrons and holes recombination of Cs₃BiBr₆ and Cs₃Bi₂Br₉ and the indirect bandgap of Cs₃Bi₂Br₉, respectively.^[25,26] Two absorption peaks centered near 380 and 450 nm can be ascribed to the bandgap of Cs₃BiBr₆ and Cs₃Bi₂Br₉, respectively (Figure S7, Supporting Information).^[27,28]

Cross-sectional transmission electron microscopy (TEM) images and the corresponding EDS mappings are shown in Figure 1e–h. The upper Bi- and Br-rich layer can be indexed to Cs₃Bi₂Br₉ and the lower layer may be ascribed to Cs₃BiBr₆ and Cs₃Bi₂Br₉ composites. High-resolution TEM (HRTEM) imaging and selected area electron diffraction pattern (Figure 1i–l) were performed to further prove the crystallization shown in Figure 1e. Clear lattice fringes with an interplanar lattice spacing of 0.29 and 0.31 nm (Figure 1j) correspond to the (103) planes of Cs₃Bi₂Br₉ and the (004) planes of Cs₃BiBr₆, respectively, indicating that the lower layer is made up of polycrystalline Cs₃BiBr₆ and Cs₃Bi₂Br₉. The lattice spacing of 0.98 nm (Figure 1k) corresponds to the (001) planes of Cs₃Bi₂Br₉, proving the upper layer is made up of single crystalline Cs₃Bi₂Br₉ with [001] growth direction. All these characterizations indicate the successful fabrication of Cs₃BiBr₆ and Cs₃Bi₂Br₉ bulk heterojunction.

Two different structures photodetectors were named as PD1 (horizontal) and PD2 (portrait), as shown in Figure S2, Supporting Information. The photoelectric properties of PD1 and PD2 were investigated in ambient condition by using two-probe methods. Figure S8a,b, Supporting Information shows the current–voltage (*I*–*V*) curves of PD1 and PD2, respectively, in the dark and light (360 and 450 nm) conditions. The results clearly show that both of the PDs are sensitive to 360 and 450 nm light. PD2 demonstrates obvious rectifying behavior (in dark) and enhanced photocurrent which may be due to the asymmetric electrode. Figure S9a,b, Supporting Information is the corresponding current–time (*I*–*t*) curves under 2-V bias, showing good stability and periodicity of the two PDs, under both 360 and 450 nm light.

The spectral responsivity ($R = \frac{I_1 - I_d}{PA}$, where *I*₁ is the light current, *I*_d is the dark current, *P* is the power density,

and *A* is the effective light area) indicates how efficiently a detector responds to optical signals.^[29] The spectral detectivity

$$(D^* = \frac{R}{(2eI_d / A)^{1/2}}, e = 1.6 \times 10^{-19} \text{ C})$$

reflects the ability to detect weak signals from a noisy environment.^[30] These parameters were used to evaluate the performance of PD1 and PD2. Figure S10 and S11, Supporting Information shows the spectral response *I*–*t* curves of PD1 and PD2, respectively. Figure 2a,b shows the *R* (left axis) and *D*^{*} (right axis) values for PD1 and PD2, respectively, at 2 V bias. Both PDs exhibit dual-band photodetection ability with peak *R* and *D*^{*} values centered at 360 and 450 nm, respectively. PD2 exhibited an *R* of 225.5 mA W⁻¹ (at 360 nm) and 10.7 mA W⁻¹ (at 450 nm), which is 29.3 and 8.9 times of that of PD1 with an *R* of 7.7 mA W⁻¹ (at 360 nm) and 1.2 mA W⁻¹ (at 450 nm). In the meantime, the *D*^{*} values of PD2 were 1.7 × 10¹² Jones (at 360 nm) and 8.7 × 10¹⁰ Jones (at 450 nm) which is 5.8 and 1.9 times of that of PD1 with *D*^{*} of 2.9 × 10¹¹ Jones (at 360 nm) and 4.5 × 10¹⁰ Jones (at 450 nm).

The *I*–*t* curves of PD1 and PD2 with respect to the increased light intensities are shown in Figures S12 and S13, Supporting Information, respectively. The photocurrent values of both PDs increase as the light intensities increase, which matches well with the fact that the photo-generation efficiency of charge carriers is proportional to the absorbed photon flux. The corresponding dependence of photocurrent on light intensity ($I = P^\theta$)^[31] is shown in Figure 2c. The value θ (0.5 < θ < 1) determines the response of photocurrent to light intensity, depending on the processes of electron-hole generation, trapping, and recombination. The values of θ were calculated as 0.86 and 0.69 for PD2 and PD1, respectively. The large θ value of PD2 means that the photo-generated carriers are less recombined, which may be due to the reduced electrode distance and asymmetric electrode. The shorter electrode distance reduces the probability of carriers being trapped, and the potential difference between asymmetric electrodes accelerates the transport of electrons and holes. Figures S14 and S15, Supporting Information show the *I*–*t* curves of PD1 and PD2 under different voltage conditions (with 360 nm light at 2.09 mW cm⁻²). It can be seen that the responsivity is enhanced with the increase of applied voltage; however, the on/off ratio is decreased.

The photodetection ability of PD2 under 0-V bias was further characterized to evaluate its self-powered performance. Figure 2c shows the *I*–*t* curves of PD2 performed at different light intensities (360 nm; 0 V). The photocurrent increased with the increasing UV light intensity while the dark current was almost unchanged. The corresponding on/off ratio is increased from 818 (0.03 mW cm⁻²) to 18881 (2.09 mW cm⁻²) and the corresponding fitted θ is 0.79, as illustrated in Figure S16, Supporting Information.

Figure S17, Supporting Information shows the *I*–*t* curve of the spectral response of PD2 under 0-V bias; the calculated *R* (left axis) and *D*^{*} (right axis) values are shown in Figure 2e. High self-powered *R* values of 59.4 mA W⁻¹ (at 360 nm) and 3.09 mA W⁻¹ (at 450 nm) and *D*^{*} values of 1.2 × 10¹² Jones (at 360 nm) and 6 × 10¹⁰ Jones (at 450 nm) were attained. The external quantum efficiency (EQE; $EQE = \frac{R \cdot \lambda}{1.24} \times 100\%$; *R* is in units of mA W⁻¹, λ is the wavelength of light)^[32] denotes the

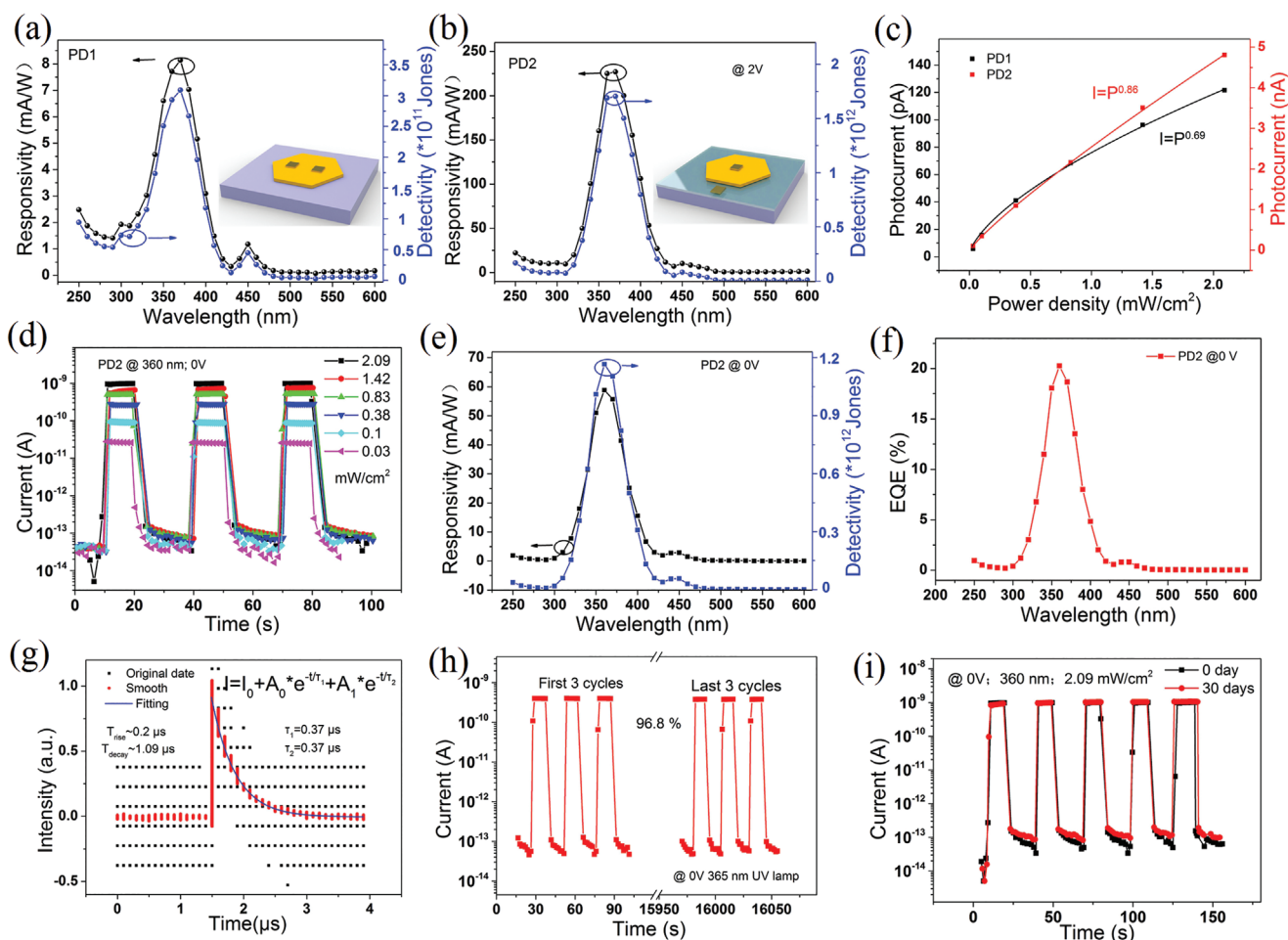


Figure 2. a,b) Responsivity and detectivity spectra for the PD1 and PD2, respectively, at 2 V; the inset shows the corresponding structure of PD1 and PD2. c) Photocurrent of PD1 and PD2 as a function of light intensity. d) $I-t$ curves of PD2 under varying UV light (360 nm) intensity at 0 V. e,f) Responsivity, detectivity, and external quantum efficiency (EQE) spectra of PD2 (360 nm; 0 V). g) Transient photoresponse for the PD2 under excitation of a 355 nm pulsed laser. h) First and last three cycles of 700 cycles of $I-t$ curves of PD2 under a 365 nm UV lamp. i) $I-t$ curves of PD2 measured after 30 days.

number of electrons and holes produced by an incident photon. A high EQE of 20.37% was achieved at 360 nm UV light (0 V), as shown in Figure 2f.

Fast response speed to light signals is crucial to high-performance PDs. Figure 2g shows the pulse response of PD2, and Figure S18, Supporting Information shows the photoresponse measurement system. The PD exhibits state-of-the-art response speed with a rise time of 200 ns and decay time of 1.09 μ s. The decay time can be fitted by the equation: $I = I_0 + A_0 \cdot e^{-t/\tau_1} + A_1 \cdot e^{-t/\tau_2}$.^[33] The fitting τ_1 and τ_2 values are both 370 ns, demonstrating the fast recombination speed of electrons and holes when the light is off. The performance of our PD is better than that of other literature reports, as shown in Table S1, Supporting Information.

In practical applications, stability is another significant parameter for perovskite PDs. Continuous illumination and environmental stability hinder long-term operation of the PDs.^[34] To determine the performance stability of the as-prepared CBB photodetectors, we first investigated the stability under continuous ultraviolet illumination with a 365 nm UV lamp. The PD2 maintained 96.8% photodetection ability after 700 cycles

($\approx 16\ 000$ s) of continuous measurement, as shown in Figure 2h and Figure S19, Supporting Information. In addition, steady performance with only a small amplitude decay was achieved even after 30 days (Figure 2i). Furthermore, a flexible PD1-type dual-band PD with a certain degree of flexibility was fabricated on a PET substrate and exhibited good photodetection ability (Figure S20, Supporting Information), meeting the demands for flexible devices. The high performance and stability of CBB-based PDs shed light on their application in light communication and imaging prospects.

PD2 showed excellent self-powered photoresponse to UV (360 nm) and visible light (450 nm). The photocurrent signals could be regulated by the wavelength and intensity of incident light. The PD as the receiving terminal of the optical signal could output different photocurrent states under both pulsed light. When the PD was illuminated by 360 nm light, the output electrical signals were defined as “■” and the electrical signals was defined as “•” when it was illuminated by 450 nm light (Figure 3a). A series of changing light signals was illuminated on the PD, resulting in the electrical signals shown in Figure 3b, in which the current of approximately 400 pA is

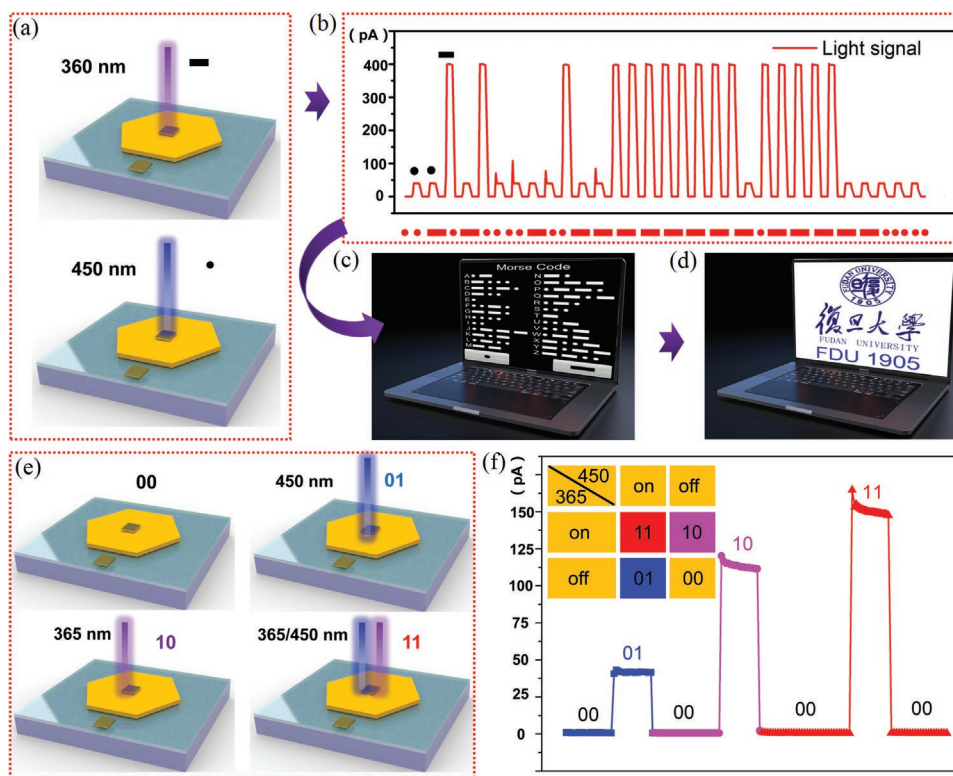


Figure 3. a) Schematic diagram of the PD2 under monochromatic light, respectively. b) $I-t$ curve of PD2 under a specific period of light and the corresponding light signal. c) The Morse Code. d) Result analyzed from the light signal of (b). e) Schematic diagram of the PD2 under dark, 360, 450, and mixed light (360 and 450 nm). f) $I-t$ curves corresponding to the condition of (e).

denoted “■” and the current of ≈ 50 pA is denoted “•”. When decoding the current signals by Morse code (Figure 3c), the

message “FDU 1905” was obtained (Figure 3d). Furthermore, the output current under dark, monochromatic UV, or visible light and the mixed light (schematics shown in Figure 3e) is shown in Figure 3f; the photocurrent under the mixed light was the linear superposition of the photocurrent under monochromatic UV or visible light. Thus, the signals “00”, “01”, “10”, and “11” can be controlled by turning on and off specific incident light, as shown in the inset of Figure 3f, demonstrating a great application prospect of our PD in modern communication technology.

In order to explore the possibility of the CBB heterostructure-based PD for device integration applications, the PD’s light imaging capabilities were explored. As schematically shown in Figure 4a, gold electrode arrays were fabricated on the surface CBB surface (unit electrode size $50 \times 50 \mu\text{m}$; the transmittance is shown in Figure S21, Supporting Information). While keeping the testing system still, the current of each device unit was recorded one-by-one by traveling one probes connecting with the top Au electrode. We tested the CBB photoresponse current under UV (360 nm) and visible (450 nm) light in the shape of the letters “FDU”, as shown in Figure 4b. Careful analysis found that all device units had dark current with an average value of $\approx 10^{-14}$ A, and an average photocurrent values of $\approx 10^{-10}$ A (360 nm) and $\approx 10^{-11}$ A (450 nm), at a bias of 0 V and the data is given in Figure S22 and Tables S2, Supporting Information. After measurement of all units, the results were described by a 2D current contrast map. Significantly, as observed in Figure 4c,d, the shape of “FDU” could be clearly identified when the device was illuminated by 360 or 450 nm light, which

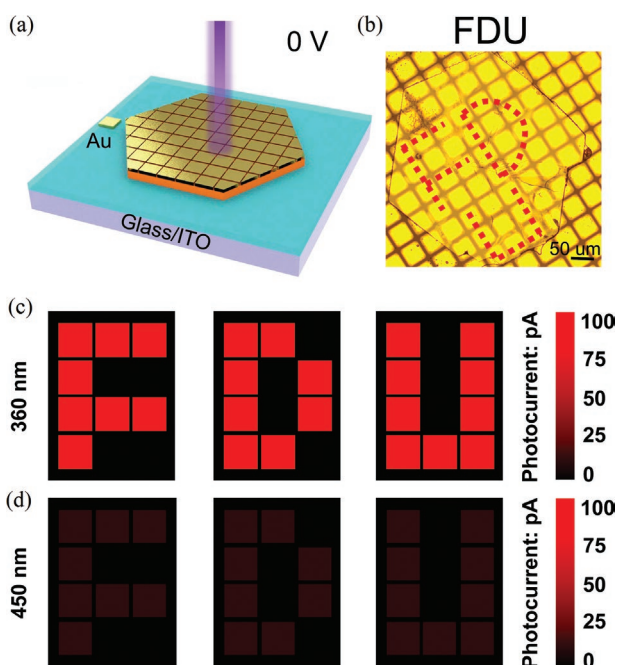


Figure 4. a,b) Schematic diagram and optical photographs of the imaging device. c,d) Imaging results of PD2 under 360 nm (2.09 mW cm^{-2}) and 450 nm (2.05 mW cm^{-2}) light, respectively.

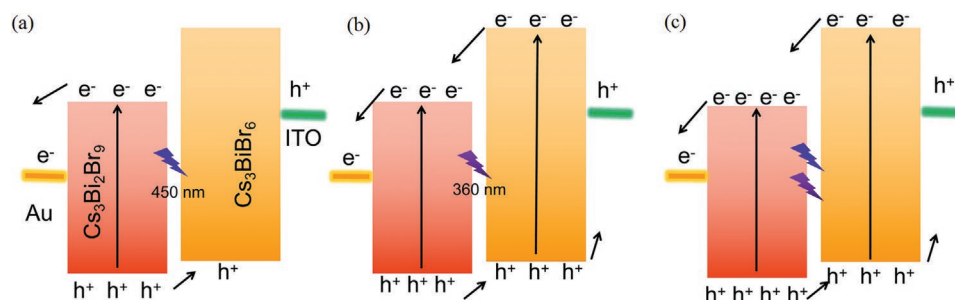


Figure 5. Proposed mechanism of photo-generated carriers transfer between $\text{Cs}_3\text{Bi}_2\text{Br}_9$ and Cs_3BiBr_6 heterostructure under a) 450 nm, b) 360 nm, and c) mixed light (450 and 360 nm) irradiation.

implies that the preliminary dual-band light imaging function of the CBB-based PDs may meet the demands of the third-generation imaging technology. The narrow fluctuations of the photocurrent further suggested a uniform photo-response performance. Such a good uniformity of the device performance can be attributed to the small variation of the CBB bulk heterostructure, which also suggests a great potential for integrated device applications.

The crystal structures of $\text{Cs}_3\text{Bi}_2\text{Br}_9$ and Cs_3BiBr_6 are illustrated in Figure S25a, Supporting Information and the corresponding Brillouin zone and high-symmetry points are shown in Figures S23 and S24, Supporting Information, respectively. Band structures and the partial and total density of states (PDOS/TDOS) for $\text{Cs}_3\text{Bi}_2\text{Br}_9$ and Cs_3BiBr_6 were simulated using the density functional theory method as shown in Figure S25b–e.^[35–38] The direct band gap value was calculated as approximately 2.59 eV for $\text{Cs}_3\text{Bi}_2\text{Br}_9$ and 3.42 eV for Cs_3BiBr_6 . The simulated band gap values differed little from those of the experimental results (2.69 eV for $\text{Cs}_3\text{Bi}_2\text{Br}_9$ and 3.26 for Cs_3BiBr_6), which may be resulted from the well-known limitation of GGA.^[39] A flatter energy band is associated with stronger localization of the charge carriers. Thus, the mobility of both electrons and holes in Cs_3BiBr_6 is lower than that of $\text{Cs}_3\text{Bi}_2\text{Br}_9$. Furthermore, the valence band maximum (VBM) of $\text{Cs}_3\text{Bi}_2\text{Br}_9$ originated mainly from Bi 6s and Br 4p, and the conduction band minimum (CBM) is attributed mainly to Bi 6p and Br 4p. The VBM of Cs_3BiBr_6 is composed mainly of Bi 6s and Br 4p, and the CBM is composed mainly of Bi 6p, Br 4p, and Cs 6s.

The flat-band potentials of semiconductors are calculated by applying the Mulliken electronegativity theory for atoms ($\chi = \frac{I + A}{2}$; where χ is electronegativity of atoms, I and A represents first ionization energy and electron affinity, respectively) as follows:^[35] $E_{\text{CB}} = \chi_{\text{p}} - E^{\circ} - 1/2E_{\text{g}}$ and $E_{\text{VB}} = E_{\text{CB}} + E_{\text{g}}$. Here E_{CB} and E_{VB} are position VBM and CBM, respectively; χ_{p} represents the electronegativity and can be estimated by the geometric mean of the electronegativity of the constituent atoms; E° is the energy of free electrons on the hydrogen scale (≈ 4.5 eV) and E_{g} is the energy bandgap. The calculated results for $\text{Cs}_3\text{Bi}_2\text{Br}_9$ and Cs_3BiBr_6 are summarized in Tables S3 and S4, Supporting Information. The flat-band position for $\text{Cs}_3\text{Bi}_2\text{Br}_9/\text{Cs}_3\text{BiBr}_6$ is schemed in Figure S25f, Supporting Information, and a staggered type II band alignment is formed. The CBB Fermi level was calculated by Scanning Kelvin probe force microscopy with an values of approximately 4.94 eV (Figure S26, Supporting Information).

The schematic of the new structure bulk-heterojunction is illustrated in Figure S27, Supporting Information. When the PD was illuminated by monochromatic visible light (450 nm, Figure 5a), only the electrons at the valence band (VB) of $\text{Cs}_3\text{Bi}_2\text{Br}_9$ were excited to the conduction band (CB), and the holes generated at the VB will be transmitted to the VB of Cs_3BiBr_6 . Electrons were generated in both of $\text{Cs}_3\text{Bi}_2\text{Br}_9$ and Cs_3BiBr_6 , when illuminated by monochromatic UV light is on (360 nm, Figure 5b). Furthermore, the electrons were transmitted to the CB of $\text{Cs}_3\text{Bi}_2\text{Br}_9$ from Cs_3BiBr_6 , while the holes in the VB were transmitted in the opposite direction. This phenomenon contributes to the dual-band photodetection of the PD. When mixed light (360 and 450 nm) is used, there will be more carriers are generated in the PD, as shown in Figure 5c, enhancing the photocurrent of the PD when it is illuminated by mixed light.

3. Conclusion

Ultra-high performance, self-powered, and dual-band photo-detectors based on lead-free $\text{Cs}_3\text{Bi}_2\text{Br}_9/\text{Cs}_3\text{BiBr}_6$ perovskite bulk heterojunction were successfully fabricated by a simple one-step spatial confinement method. The PD possesses a UV main band with a self-powered peak responsivity of 59.4 mA W^{-1} at 360 nm and a visible sub-band with a peak responsivity of 3.09 mA W^{-1} at 450 nm. A high on/off ratio (18881), fast response speed (rise time 200 ns; decay time 1.09 μs), high detectivity (1.2×10^{12} Jones), and cycle stability were realized under the UV band at 0 V bias. Furthermore, the proposed dual-band PD can be well applied in the encrypted communication and image sensing fields. Our results open a new frontier in the search for novel dual-band high-performance PDs based on lead-free perovskite bulk heterojunction featuring structural diversity.

Supporting Information

Supporting Information is available from the Wiley Online Library or from the author.

Acknowledgements

This work is supported by the National Key R&D Program of China (No. 2017YFA0204600), the Inner Mongolia Talent Fund, the National Natural Science Foundation of China (No. 12061131009 and 51872050), the Young Scientist Project of MOE innovation platform, Science and

Technology Commission of Shanghai Municipality (No. 21520712600 and 19520744300).

Conflict of Interest

The authors declare no conflict of interest.

Data Availability Statement

Research data are not shared.

Keywords

dual-band photodetection, encrypted communication, imaging, lead-free perovskites, perovskite bulk heterojunction, self-powered devices

Received: April 4, 2022

Revised: May 23, 2022

Published online: July 10, 2022

- [1] a) M.-B. Lien, C.-H. Chun, Y. Ravishankar, S. Nien, H. Zhou, M. Fessler, J. A. Zhong, Z. Norris, B. Theodore, *Nat. Photonics* **2020**, *14*, 143; b) Y. Yang, *Nat. Electron.* **2021**, *4*, 631; c) Y. H. Chen, L. X. Su, M. M. Jiang, X. S. Fang, *J. Mater. Sci. Technol.* **2022**, *105*, 259.
- [2] L. Li, H. Y. Chen, Z. M. Fang, X. Y. Meng, C. T. Zuo, M. L. Lv, Y. Z. Tian, Y. Fang, Z. Xiao, C. X. Shan, Z. G. Xiao, Z. W. Jin, G. Z. Shen, L. Shen, L. M. Ding, *Adv. Mater.* **2020**, *32*, 1907257.
- [3] Y. C. Bu, J. P. Xu, S. B. Shi, J. Chen, M. H. Li, Q. Y. Zhang, P. C. Yang, J. H. Xu, X. S. Zhang, L. N. Kong, L. Li, *J. Mater. Chem. C* **2021**, *9*, 9203.
- [4] Z. K. Gu, C. Li, M. Z. Li, Y. L. Song, *Sci. Adv.* **2018**, *4*, eaat2390.
- [5] J. Kim, C. Jo, M.-G. Kim, G.-S. Park, T. J. Marks, A. Facchetti, S. K. Park, *Adv. Mater.* **2021**, *34*, 2106215.
- [6] W. Yang, K. Hu, F. Teng, J. Weng, Y. Zhang, X. S. Fang, *Nano Lett.* **2018**, *18*, 4697.
- [7] a) F. Cao, L. Li, *Adv. Funct. Mater.* **2021**, *31*, 2008275; b) W. D. Song, J. Chen, Z. Li, X. S. Fang, *Adv. Mater.* **2021**, *33*, 2101059.
- [8] a) B. W. Baugher, H. O. Churchill, Y. Yang, P. Jarillo-Herrero, *Nat. Nanotechnol.* **2014**, *9*, 262; b) T. T. Yan, S. Cai, Z. J. Hu, Z. Q. Li, X. S. Fang, *J. Phys. Chem. Lett.* **2021**, *12*, 9912; c) J. X. Chen, X. Y. Liu, Z. Q. Li, F. Cao, X. Lu, X. S. Fang, *Adv. Funct. Mater.* **2022**, *32*, 2201066.
- [9] D. T. You, C. X. Xu, J. Zhao, F. F. Qin, W. Zhang, R. Wang, Z. L. Shi, Q. N. Cui, *Adv. Opt. Mater.* **2019**, *7*, 1801522.
- [10] Y. Zhang, W. Xu, X. Xu, J. Cai, W. Yang, X. S. Fang, *J. Phys. Chem. Lett.* **2019**, *10*, 836.
- [11] F. Cao, L. Meng, M. Wang, W. Tian, L. Li, *Adv. Mater.* **2019**, *31*, 1806725.
- [12] Z. Q. Li, X. Liu, C. Zuo, W. Yang, X. S. Fang, *Adv. Mater.* **2021**, *33*, 2103010.
- [13] H. Kim, W. Kim, Y. Pak, T. J. Yoo, H. W. Lee, B. H. Lee, S. Kwon, G. Y. Jung, *Laser Photonics Rev.* **2020**, *14*, 2000305.
- [14] B. Yang, J. S. Chen, F. Hong, *Angew. Chem., Int. Ed.* **2017**, *56*, 12471.
- [15] W. Kim, H. Kim, T. J. Yoo, J. Y. Lee, J. Y. Jo, B. H. Lee, A. A. Sasikala, G. Y. Jung, Y. Pak, *Nat. Commun.* **2022**, *13*, 720.
- [16] S.-X. Li, Y.-S. Xu, C.-L. Li, Q. Guo, G. Wang, H. Xia, H.-H. Fang, L. Shen, H.-B. Sun, *Adv. Mater.* **2020**, *32*, 2001998.
- [17] J. G. Feng, C. Gong, B. Zhang, Y. C. Wu, H. F. Gao, Y. S. Wu, W. Wen, H. B. Fu, Y. J. Gong, L. Jiang, X. Zhang, X. Y. Jiang, *Nat. Electron.* **2018**, *1*, 404.
- [18] R. S. Kei Hirose, J. Hernlund, *Science* **2017**, *358*, 734.
- [19] X. M. Chen, G. D. Scholes, W.-G. Lu, J. L. Tang, Y. Y. Zhang, Y. T. Wang, H. Z. Zhong, *Nat. Photonics* **2021**, *15*, 813.
- [20] Y. Fang, Q. Dong, Y. Shao, Y. Yuan, J. Huang, *Nat. Photonics* **2015**, *9*, 679.
- [21] J. Y. Huang, C. Dong, Y. T. Mei, X. Y. Lu, G. T. Yue, Y. Y. Gao, R. Liu, W. F. Zhang, F. R. Tan, *J. Mater. Chem. C* **2021**, *9*, 14217.
- [22] S. K. Shill, F. Wang, Z. Lai, Y. Meng, Y. Wang, D. X. Zhao, M. K. Hossain, K. Egbo, Y. Wang, K. M. Yu, J. C. Ho, *Nano Res.* **2021**, *14*, 4116.
- [23] H. Yang, T. Cai, E. Liu, K. Hills-Kimball, J. Gao, O. Chen, *Nano Res.* **2019**, *13*, 282.
- [24] M. N. Tran, I. J. Cleveland, E. S. Aydil, *J. Mater. Chem. C* **2020**, *8*, 10456.
- [25] L. Y. Lian, G. M. Zhai, F. Cheng, Y. Xia, M. Y. Zheng, J. P. Ke, M. Y. Gao, H. Liu, D. L. Zhang, *CrystEngComm* **2018**, *20*, 7473.
- [26] M. N. Tran, I. J. Cleveland, G. A. Pustorino, E. S. Aydil, *J. Mater. Chem. A* **2021**, *9*, 13026.
- [27] Y. H. Zhang, J. Yin, M. R. Parida, G. H. Ahmed, J. Pan, O. M. Bakr, J.-L. Brédas, O. F. Mohammed, *J. Phys. Chem. Lett.* **2017**, *8*, 3173.
- [28] Z. Ji, Y. Liu, W. Li, C. Zhao, W. Mai, *Sci. Bull.* **2020**, *65*, 1371.
- [29] W. Ouyang, F. Teng, X. S. Fang, *Adv. Funct. Mater.* **2018**, *28*, 1707178.
- [30] a) B. Zhao, F. Wang, H. Y. Chen, Y. P. Wang, M. M. Jiang, X. S. Fang, D. X. Zhao, *Nano Lett.* **2015**, *15*, 3988; b) B. Zhao, F. Wang, H. Y. Chen, L. X. Zheng, L. X. Su, D. X. Zhao, X. S. Fang, *Adv. Funct. Mater.* **2017**, *27*, 1700264.
- [31] F. Cao, L. Jin, Y. Wu, X. Ji, *J. Alloys Compd.* **2021**, *859*, 158383.
- [32] a) R. D. Tang, S. C. Han, F. Teng, K. Hu, Z. M. Zhang, M. X. Hu, X. S. Fang, *Adv. Sci.* **2018**, *5*, 1700334; b) X. J. Xu, J. X. Chen, S. Cai, Z. H. Long, Y. Zhang, L. X. Su, S. S. He, C. Q. Tang, P. Liu, H. S. Peng, X. S. Fang, *Adv. Mater.* **2018**, *30*, 1803165.
- [33] F. Cao, Z. Pan, X. Ji, *J. Appl. Phys.* **2021**, *129*, 204503.
- [34] X. N. Zhang, X. Y. Liu, B. Sun, H. B. Ye, C. H. He, L. X. Kong, G. L. Li, Z. Y. Liu, G. L. Liao, *ACS Appl. Mater. Interfaces* **2021**, *13*, 35949.
- [35] X. Meng, Z. Li, H. Zeng, J. Chen, Z. Zhang, *Appl. Catal., B* **2017**, *210*, 160.
- [36] P. Hohenberg, W. Kohn, *Phys. Rev.* **1964**, *136*, B864.
- [37] G. Kresse, J. Furthmüller, *Phys. Rev. B* **1996**, *54*, 11169.
- [38] J. P. Perdew, K. Burke, M. Ernzerhof, *Phys. Rev. Lett.* **1996**, *77*, 3865.
- [39] B.-H. Wang, B. Sun, L. Chen, M.-Q. Cai, S.-F. Yin, *J. Phys. Chem. C* **2021**, *125*, 13212.